Title

Experimental investigation of injection-induced fracturing during supercritical CO2 sequestration

Authors

Wang, Lei
Yao, Bowen
Xie, Haojun
et al.

Publication Date

2017-08-01

DOI

10.1016/j.ijggc.2017.05.006

Peer reviewed

Experimental investigation of injection-induced fracturing during supercritical CO_2 sequestration

Lei Wang[a], Bowen Yao[a], Haojun Xie[b], Timothy J. Kneafsey[c],

Philip H. Winterfeld[a], Xiaolong Yin[a], Yu-Shu Wu[a].

[a]Petroleum Engineering Department, Colorado School of Mines, [b]College of Petroleum Engineering, China University of Petroleum (East China), [c]Earth Science Division, Lawrence Berkeley National Laboratory.

The first two authors have equal contribution to the experiments.

Abstract

Leakage risk assessment is an inevitable procedure in permanent sequestration and storage of CO_2 in deep saline aquifers and depleted oil and gas reservoirs, where the integrity of caprock is most critical. Low porosity and low permeability concrete cubes were employed as caprock analogs to investigate the supercritical CO_2 injection-induced fracturing processes under true tri-axial stress conditions. A systematic experimental procedure, consisting of active acoustic emission measurement, pressure decay, injection pressure and temperature monitoring, fracture coloring, and gas fracturing, is formulated to qualitatively and quantitatively characterize the injection-induced fracturing processes and fracture morphology. Occurrence of injection-induced fracturing can be directly identified from peaks of borehole pressure profiles as well as sharp drops on temperature profiles due to CO_2 expansion, but generally there was no fracture propagation plateau appearing for the 20 cm rock cubes with zero pore pressure. Acoustic wave signatures, including both waveform change and arrival time delay, can effectively capture the extension of induced fractures inside the opaque rock. Initiation and propagation of supercritical CO_2 injection-induced fractures are highly dominated by the tri-axial stresses, following the general trend of continuum mechanics at high stress levels with large stress difference. As the stress difference decreases, induced fractures branch off in relatively arbitrary directions. For these supercritical CO_2 injection-induced fracturing experiments, poroelastic mechanics model makes a decent fit with the measured breakdown pressure of the caprock analogs. Findings in this study are valuable for risk analysis and operation optimization of geological CO_2 sequestration and storage as well as for CO_2 fracturing design and implementation in shale and tight reservoirs.

Keywords: CO_2 sequestration and storage; supercritical CO_2; fracturing; geomechanics; true tri-axial stress; caprock

I. Introduction

Geologic storage is a practical means for sequestrating large amounts of CO_2 for long-term purpose [Ehlig-Economides 2010, Leung et al. 2014]. Saline aquifers and conventional oil and gas reservoirs are considered as the most prospective candidate sites for CO_2 geologic storage, seeing that they are pervasive around the world and are mostly well sealed by low permeability overlying caprock, commonly referred as shale. Apparently, injecting large amounts of CO_2 into geologic reservoirs brings about elevated pressure and significant changes in in-situ stress states, which could possibly reactivate existing natural fractures / faults or even create new fractures in the caprock [Lee et al. 2012]. Such high conductivity pathways, once break through the caprock,

could result in CO_2 seeping upward into other formations or further overflowing to the surface. Since typically the reservoir pressure and temperature are above the critical pressure 7.38 MPa (1070.4 psi) and temperature 31.0 ºC (304.2 K) of CO_2 [Suehiro et al. 1996], sequestered CO_2 is supercritical with properties midway of the gas and liquid states. For instance, in the In Salah CO_2 storage project, the bottomhole temperatures and pressures of injection wells KB 501 and 503 were around 55 ºC and were generally above 3600 psi (Bissell et al. 2011). To meet the goals of developing and validating technologies to ensure 99% storage permanence and supporting industry to predict CO_2 storage capacity in geologic formations within 30% [DOE, 2014], evaluation of the integrity or proper design of a supercritical CO_2 ($scCO_2$) flow and geologic storage system is critical for a large amount injection and safe storage for a long time. Thus, there is a need to understand the formation of leakage pathways and the enhancement of flow through those pathways in sealing formations caused by $scCO_2$ injection-induced fracturing and associated geomechanical effects.

$scCO_2$ injection-induced fracturing

Existing natural fractures can be reactivated and new fractures can be created by injecting fluids into storage or sealing formations at high pressure, commonly referred as hydraulic fracturing, which is a common process in developing shale and tight reservoirs in the oil and gas industry these days. Initiation and propagation of fractures have been extensively studied within the context of hydraulic fracturing using water, oil, or polymer gels. [Daneshy 1978, Warpinski et al. 1982, Weijers et al. 1996, Bunger et al. 2005, Wang et al. 2016]. Liquid CO_2, as a fracturing fluid, has also been injected at high flow rate and pressure to fracture tight oil and gas reservoirs. It is estimated that in North America over 1,000 wells in tight sandstone and shale formations have been fractured using liquid CO_2 since the 1980s [Lillies and King 1982, Sinal and Lancaster 1987, Gupta and Bobier 1998]. In these field practices, liquid CO_2 was gelled to achieve high viscosity up to tens of centipoises [King 1983, Gupta et al. 2003], by which sand proppant was suspended for propping up the generated hydraulic fractures. Hydrocarbons are then able to flow out of the rock matrix into fractures and converge to the wellbore more easily.

Regarding sequestration and storage of $scCO_2$ in geologic formations, the objective of avoiding fracturing sealing formation is opposite to that of hydraulic fracturing. Still, obtaining the fracture initiation condition as well as the dynamics of fracture propagation induced by $scCO_2$ injection pressure in sealing formation is the utmost priority for leakage risk analysis, simulation prediction, and field implementation [Rinaldi and Rutqvist 2013, Huang et al. 2015, Wang et al. 2016]. However, when the injected fluid is pure liquid or supercritical CO_2, laboratory experiments on evaluating the sealing rock fracturing behaviors are relatively rare. Ishida et al. [2012] injected liquid and supercritical CO_2 into 17 cm granite cubes to compare the fracturing behaviors under hydrostatic stress of 1 MPa. Based on lower breakdown pressure and more acoustic emission sources in the case of $scCO_2$, the authors suggested that fractures generated by $scCO_2$ are more wavelike and have more branches than those by liquid CO_2, attributing to the lower viscosity of $scCO_2$. Under near reservoir conditions, Rinehart et al. [2016] investigated the chemical-mechanical responses of sandstone cores obtained from Lower Tuscaloosa Formation,

which is a CO_2 storage horizon. The chlorite-cemented cores saturated with $scCO_2$-saturated brine showed lower yielding stress and failure envelope than in-situ stress, as a possible result of the reaction between chlorite and acidic $scCO_2$-brine. In addition, there are CO_2 injection tests carried out in shallow wells in carbonate vadose zone, nonetheless, the aim was to monitor the temporal and spatial distribution of the CO_2 plume while CO_2 was injected as gas [Rillard et al. 2015, Rhino et al. 2016].

Breakdown pressure correlation

Initiation of hydraulic fractures in non-poroelastic rock is only a function of the stress state and the tensile strength of the rock according to continuum mechanics. The breakdown pressure when fluid is injected into borehole is [Hubbert and Willis 1957]

$$P_b = 3\sigma_h - \sigma_H + \sigma_t - P_p \tag{1}$$

where σ_h and σ_H are the minimum and maximum horizontal stress, respectively. And σ_t is the tensile strength of the rock, P_p is the pore pressure.

If the rock is assumed as poroelastic, then the breakdown pressure is [Haimson and Fairhurst 1967, Detournay and Cheng 1992]

$$P_b = \frac{3\sigma_h - \sigma_H + \sigma_t - \eta P_p}{2 - \eta} \tag{2}$$

where $\eta = \alpha(1-2\upsilon)/(1-\upsilon)$, a function of Biot's constant α and Poisson's ratio υ.

Breakdown pressure calculated from equation (1) is the upper bound for rock samples. The assumptions for the above equations exclude several factors, such as fluid viscosity, injection rate, rock sample size, and thermal stress, which could also affect the breakdown pressure [Schmitt and Zoback 1992, Detournay and Cheng 1993, Stoeckhert et al. 2015, Li et al. 2016]. In view of the special fluid property, whether $scCO_2$ injection-induced fracturing could be accurately quantified by these equation is unknown.

This study developed a series of quantitative experimental approaches for understanding and predicting geomechanical effects on CO_2 injection in the subsurface, and provided evaluation tools and techniques for assessing and validating CO_2 flow and risk of leakage through low permeability caprock analogs-cubic concrete blocks. Specifically, a tri-axial loading frame was employed to study fracture initiation and propagation in concrete blocks caused by $scCO_2$

injection into the centered borehole. Tri-axial stress states, injection pressure, fracture mechanical responses, permeability change of caprocks, injection-induced fracture patterns are investigated by real-time data acquisition, pressure decay tests, acoustic emission tests, and dye coloring.

II. Experimental procedures and methods

In the $scCO_2$ injection-induced fracturing experiments, we used homogeneous concrete blocks which have similar porosity, permeability, and geomechanical properties to represent the rock of the storage / caprock formations. The concrete blocks were 20 cm cubes which were prepared by mixing sand, Portland cement, and water in the mass ratio of 2.50:1.00:0.55 [Yao 2015]. It is worth mentioning that the Portland cement used was manufactured from the calcination of the Niobrara shale outcrop. After curing for more than 40 days, the average porosity and permeability of the dry concrete samples are 9.56% and 9 micro-Darcy, respectively [Alqatahni 2015]. The tensile strength measured by Brazilian tests for three cylindrical samples is 356, 488, and 576 psi, with an average of 473 psi. Borehole with diameter of 2.5 cm was first drilled from the center of one sample face to its center, i.e. 10 cm long. Then steel tubing was cemented into the borehole with epoxy to the depth of 7.5 cm, leaving the 2.5 cm bottom section uncased. Prior to the $scCO_2$ injection experiments, the concrete samples were characterized by acoustic emission and pressure decay tests, which were repeated after the injection for comparison. Supercritical CO_2 were then injected into the bore hole to build up pressure and to induce fracturing, during which the pressure and temperature in the borehole were continuously recorded. Injection rate was adjusted through the pump controller.

Specifically, for each concrete sample, the following experimental procedures were carried out:

1. Drill borehole and install wellhead into the sample,
2. Pre-injection stress loading for 40 minutes at planned tri-axial stresses,
3. Take pictures of six faces of the cubic sample,
4. Active acoustic emission measurements,
5. Borehole pressure decay tests from 180 psig under no stress loading,
6. Inject 60°C $scCO_2$ into the pre-heated 60°C concrete block under planned tri-axial stress loading until it is fractured,
7. Active acoustic emission measurements,
8. Take pictures of sample faces,
9. Borehole pressure decay from 180 psig under no stress loading,
10. Inject dye solution into the fractured sample,
11. Inject high-pressure N_2 to break down the fractured sample,
12. Take pictures of fracture planes.

In **Step 2**, tri-axial stresses were first applied for 40 minutes before any tests to attenuate the compressibility of the concrete blocks. Active acoustic emission tests employ P and S wave actuators and receivers on opposite sample faces to detect the injection-induced fractures inside the concrete samples non-destructively, based on that fractures on the way of P and S-wave transmission can affect their waveform and arrival time [Alqatahni et al. 2016]. In **Step 5**, by building up borehole pressure to 180 psig and let it drop naturally, the gas leak-off rate or the gas permeability before and after the $scCO_2$ injection can be directly reflected on pressure-time

profiles. It is worth noting that the borehole was sufficiently exposed to CO_2 in air for a few days for wellhead installation and pre-injection characterization tests, thus the carbonation reaction during $scCO_2$ injection is considered negligible in these experiments.

Injection of $scCO_2$ into concrete blocks under tri-axial stress loading in **Step 6** was carried out on an experimental system as shown in **Figure 1**, which consists of a $scCO_2$ generation and injection sub-system, a tri-axial stress loading frame, and a data logging and processing sub-system. Liquid CO_2 was transferred to the ISCO pump cylinder wrapped by a heating tape, which can heat the pump cylinder to the desired 60°C. The concrete sample was pre-heated at 60°C in an oven for 8 hours before being placed in the tri-axial loading frame, which can exert true tri-axial stresses to the desired level. Details of the tri-axial loading frame can be found in Cha et al. [2016]. The data logging and processing sub-system monitored the tri-axial stresses in x, y, and z directions as well as the borehole pressure and temperature through a pressure transducer and a thermocouple set inside the borehole in real-time.

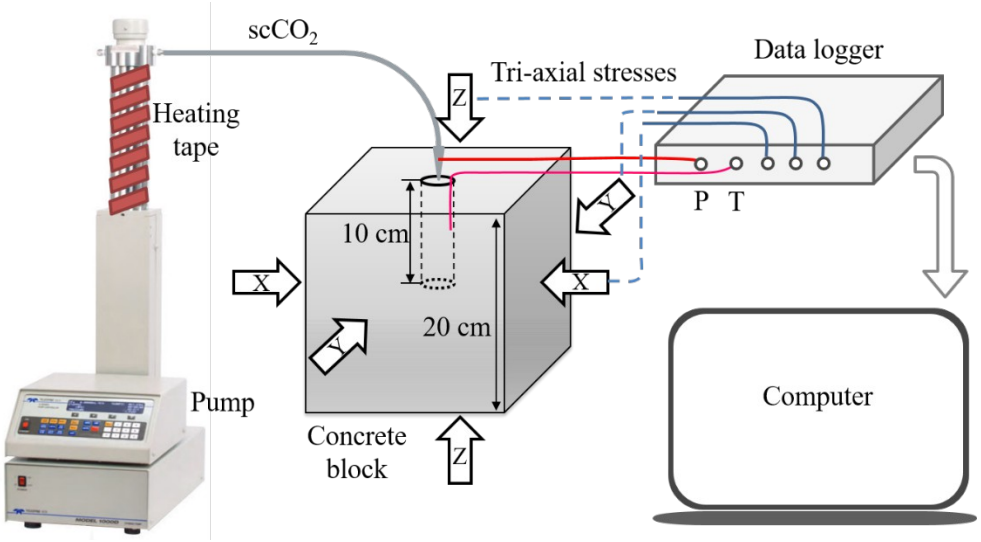

Figure 1 Experimental system for $scCO_2$ injection into a cubic concrete block.

As shown in **Figure 2**, faces of each concrete sample are numbered from 1 to 6 on their upper right corner, with x-stress loading on face 2 and 4, y-stress loading on face 1 and 3, and z-stress loading on face 5 and 6. Active acoustic emission measurement locations on face 1, 2, 3, and 4 are the same, counting from 1 to 12, as marked in the middle image, while only 8 locations were selected for face 5 and 6, as depicted in the right image. Actuators were always placed on face 1, 2, and 5, to send the signal and receivers were placed at corresponding locations on face 3, 4, and 6 to receive the signal.

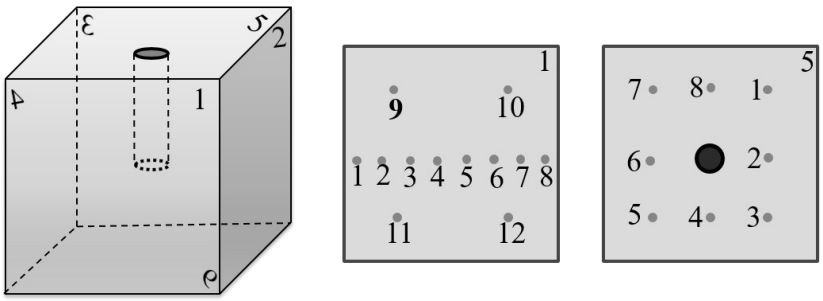

Figure 2 Acoustic emission measurement locations on concrete sample faces (left-face numbering, middle-face 1 or 2, right-face 5).

III. Results and discussion

Five concrete samples, as listed in **Table 1**, were utilized for $scCO_2$ injection-induced fracturing experiments under different tri-axial stress conditions. All the borehole pressure and temperature values were above the critical point of CO_2 when these samples were fractured. The injection rate was kept constant at 40 ml/min for all samples. Each experiment was conducted with different tri-axial stresses by first changing stress loading levels for sample 1, 2, 3, and then stress differences for sample 4 and 5.

Table 1 Experimental conditions of $scCO_2$ injection for 5 concrete samples

Concrete #	Tri-axial stress x:y:z, psi	Stress difference, psi	Injection rate, ml/min
1	1000:1625:2250	625	40
2	1250:1875:2500	625	40
3	1500:2125:2750	625	40
4	1250:1562:1875	312	40
5	1250:2187:3125	937	40

Pre-treatment stress loading

All concrete samples were prepared in mold without external confining stress, leaving them compressible under tri-axial stresses of high levels, from which the resultant compressibility could interfere with the acoustic signatures caused by induced fractures. Hence, each concrete sample was loaded with tri-axial stresses for about 40 mins to partially eliminate the effect of compressibility for following acoustic measurements. **Figure 3** shows the true tri-axial stress profiles loaded onto sample 2 using air pumps. Stresses in x, y, and z directions were increased stepwise to avoid any damage to the concrete sample. The slowly relaxing stresses were exerted quasi-static. That is, to maintain the desired stress levels, air pumps were pressed occasionally, bringing about the corrugated curves. Pre-injection tri-axial stress profiles for other samples are similar, for brevity they are omitted here.

Figure 3 Pre-injection tri-axial stress loading of sample 2 for ~40 mins.

Pressure and temperature during $scCO_2$ injection

During the injection of $scCO_2$ into concrete samples, tri-axial stresses applied on the sample, and borehole pressure and temperature were continuously monitored. Note that the tri-axial stresses were continuously relaxing, thus the actual stresses applied were not exactly the same as but were close to those planned in **Table 1**. The air pumps were pressed to maintain the stresses whenever in need. In the following sections, stress relevant analyses use the actual tri-axial stress values.

Under planned tri-axial stresses of x:y:z = 1000:1625:2250 psi, sample 1 was treated by injecting $scCO_2$ into borehole at a constant rate of 40 ml/min. The tri-axial stresses and borehole pressure and temperature are shown in **Figure 4** and **Figure 5**, respectively. The concrete block was fractured at 435.1 seconds, when the injection pressure reached 1091.5 psig. This peak pressure corresponds to the responses on tri-axial stress loading in x, y, and z directions in **Figure 4**. Specifically, the x-stress was slightly humped, while y-stress and z-stress fell a little when the injection pressure peaked at 435.1 seconds, indicating that the major fracture planes were generated perpendicular to the x-axis. When the peak pressure was achieved, the borehole temperature was 46.8 °C, thus the sample was fractured under supercritical conditions. Right after the peak pressure, the borehole temperature drastically dropped by about 4 °C, due to CO_2 leakage and expansion from the borehole to the outer space. After induced fracturing, the borehole pressure quickly decreased to atmospheric pressure with leaking sound, which clearly indicated that the fractures propagated to the outer surface of the concrete block. Different from hydraulic fracturing, $scCO_2$ induced fracturing occurred instantaneously in this 20 cm concrete cube and does not have a recognizable plateau of fracture propagation after the peak on the pressure profile.

Figure 4 Tri-axial stresses for sample 1 during $scCO_2$ injection.

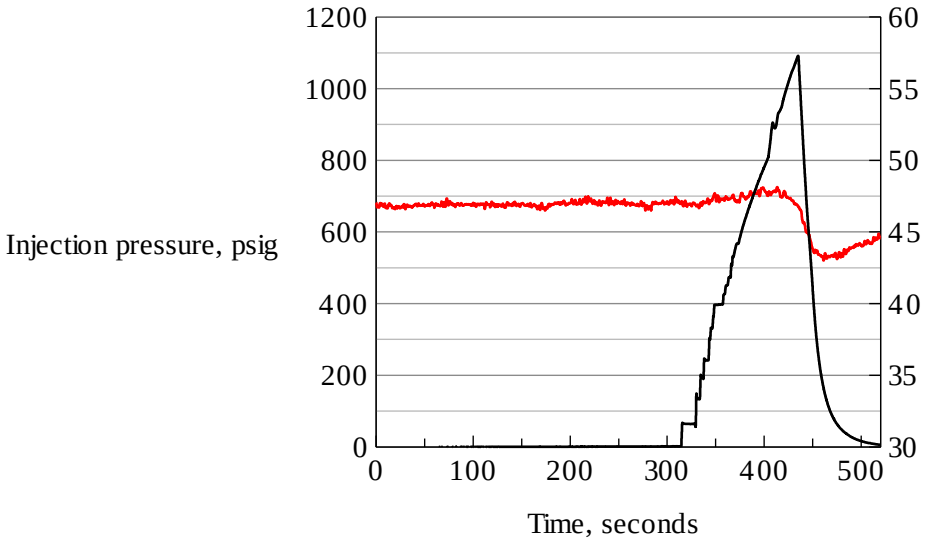

Figure 5 Borehole pressure and temperature during CO_2 injection into sample 1.

Concrete sample 2 was fractured with $scCO_2$ under planned tri-axial stresses of x:y:z = 1250:1875:2500 psi, as shown in **Figure 6**. The borehole pressure and temperature during $scCO_2$ injection are shown in **Figure 7**. On the pressure profile, there are three peaks, which come from three intermittent $scCO_2$ injection cycles due to limited volume of the pump cylinder (508 ml). After finishing injecting one pump cylinder of $scCO_2$, liquid CO_2 was transferred to the pump cylinder and heated to 60 °C before injection continued. During this time gap, the borehole pressure decreased due to $scCO_2$ leak-off. At 3669.1 seconds, the borehole pressure reached the highest peak of 1641.2 psig and started decreasing even though pump was still running at 40

ml/min. This peak pressure corresponds to the leveling-out slope on x-stress in **Figure 6**, while y-stress and z-stress did not show obvious changes, suggesting that the major induced fracture planes were created perpendicular to the x-axis. What's more, during injection x-stress decreased faster than y-stress and z-stress, which means x-stress was the primary counterbalance to the injection pressure. When the highest peak pressure was achieved, the borehole temperature was 34.8 °C, thus the sample was fractured under supercritical conditions. Around the highest pressure peak, borehole temperature only dropped about 1 °C, which is much smaller than that of sample 1. In addition, after pump stopped, the decay of borehole pressure significantly slowed down even the pressure was still above 1000 psig. These two different phenomena suggested that elevated tri-axial stress suppressed the propagation of fractures and as borehole pressure decreases, some of the fractures were closed due to high confining stress.

Figure 6 Tri-axial stresses for sample 2 during scCO_2 injection.

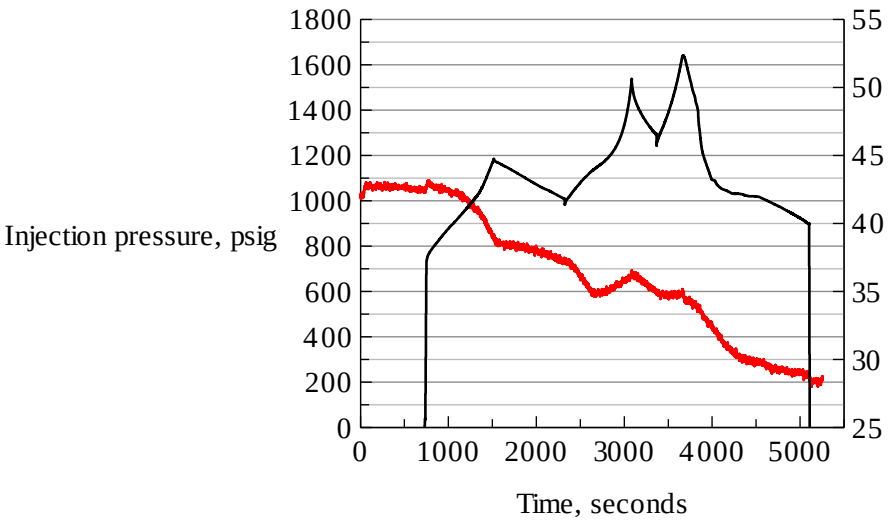

Figure 7 Borehole pressure and temperature during CO_2 injection into sample 2.

The tri-axial stresses for sample 3 was planned as x:y:z = 1500:2125:2750 psi, as shown in **Figure 8**. The borehole pressure and temperature during injection of $scCO_2$ are shown in **Figure 9**. Two cycles of $scCO_2$ were injected to induce the fracture development. The highest peak pressure of 2130.2 psig was achieved at 1006.1 seconds, after which the borehole pressure steeply decreased. This peak pressure corresponds to a noticeable hump on the x-stress in **Figure 8**, while there are no obvious responses on y-stress and z-stress, indicating that the major fracture planes were generated perpendicular to the x-axis. Around the peak pressure, the borehole temperature drastically dropped from 43.6 °C to 34.2 °C, due to fast leakage and expansion of the $scCO_2$. Also on the pressure profile, the decreasing rate slows down after the borehole pressure drops below 1250 psig, reflecting the partial closure of fractures under high confining stress conditions.

Figure 8 Tri-axial stresses for sample 3 during $scCO_2$ injection.

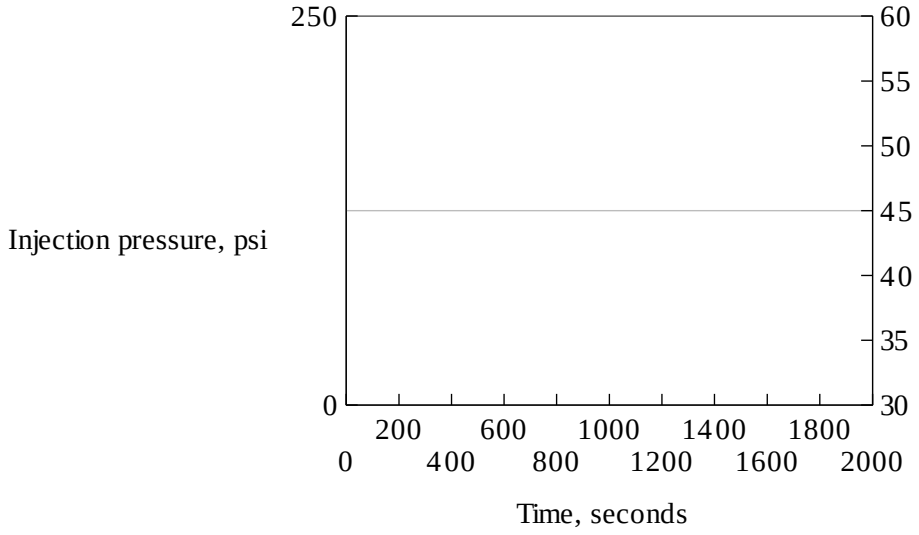

Figure 9 Borehole pressure and temperature during CO_2 injection into sample 3.

Two cycles of $scCO_2$ were injected into sample 4 under planned tri-axial stresses of x:y:z = 1250:1562:1875 psi, as shown in **Figure 10**. The borehole pressure and temperature changes during $scCO_2$ injection are shown in **Figure 11**. During the second cycle of injection, the sample was fractured with pressure reaching the highest peak of 1641.9 psig at 1217.5 seconds, when the borehole temperature experienced a sharp drop from 45.2 °C to -7.9 °C, associating with gas leaking sound. This sharp drop in temperature is a result of the fast leakage and vaporization of the high-pressure $scCO_2$. Corresponding to the fracturing occurrence, there are no remarkable fluctuations on tri-axial stress profiles, except a mild mitigation in the decreasing y-stress. This indicates that the major induced fracture planes were not perpendicular to the x-axis. Note that the

temperature first rose from the lowest point attributing to continued $scCO_2$ injection, and then dropped again because some new fractures propagated to the sample surface accelerating the $scCO_2$ leakage and evaporation.

Figure 10 Tri-axial stresses for sample 4 during $scCO_2$ injection.

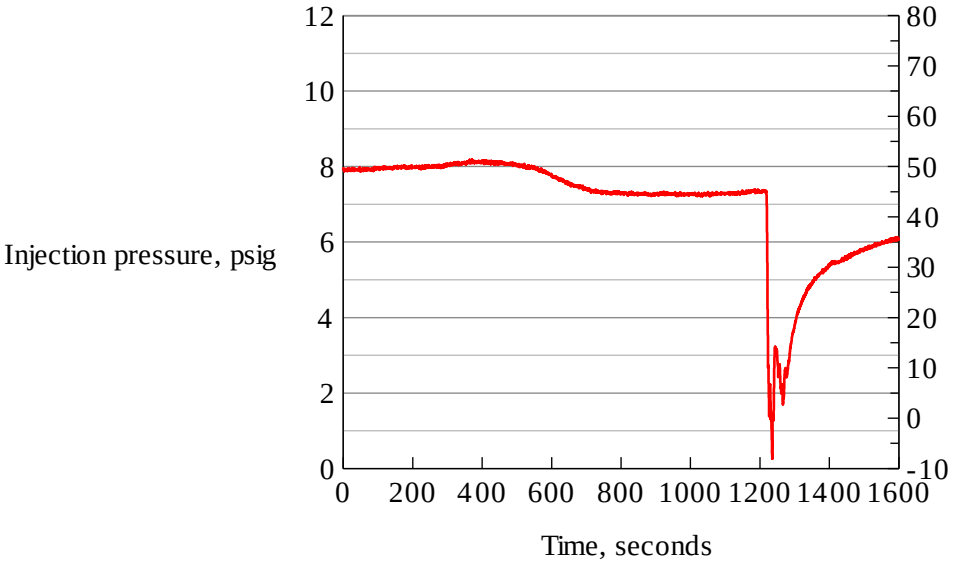

Figure 11 Borehole pressure and temperature during CO_2 injection into sample 4.

The planned tri-axial stresses applied on sample 5 for $scCO_2$ injection were x:y:z = 1250:2187:3125 psi (**Figure 12**) with the largest stress difference of 937 psi among all the experiments. The concrete sample was fractured during the second cycle of $scCO_2$ injection, with a peak pressure of 1195.5 psig at 1475.0 seconds, as shown in **Figure 13**. Also, at the fracturing

point, the borehole temperature dropped from 39.9 °C by 3.5 °C, due to $scCO_2$ leakage and vaporization. In **Figure 12**, a noticeable hump showed up on x-stress at the fracturing point, while there are no obvious changes on y-stress and z-stress profiles.

Figure 12 Tri-axial stresses for sample 5 during $scCO_2$ injection.

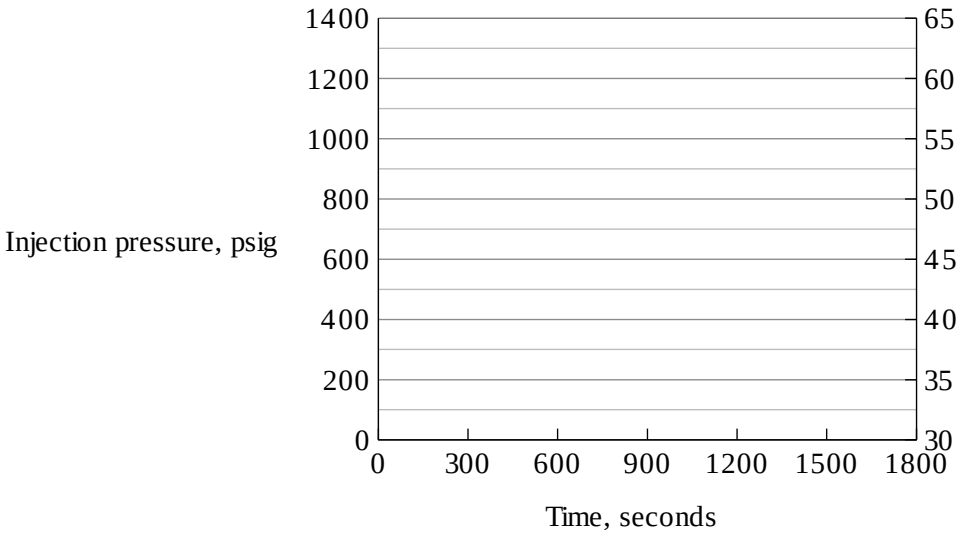

Figure 13 Borehole pressure and temperature during CO_2 injection into sample 5.

Active acoustic emission measurements

After $scCO_2$ injection, active acoustic P and S waves were measured on each pair of faces of each concrete block. These post-injection acoustic signatures are compared with pre-injection ones to examine whether fractures have been generated across the pathway connecting the actuator and receiver locations.

For concrete sample 1, the P and S-wave measurements on face 1 & 3 are shown in **Figure 14** and **Figure 15**, respectively. The black signals were measured before $scCO_2$ injection and red ones were measured afterwards. As can be seen from **Figure 14**, except location 1-3 and 9, all other locations show dramatic changes in waveforms, suggesting a major fracture plane cutting across the connecting lines between these locations on face 1 and their corresponding points on face 3. This inference is further verified by the longer arrival time delays at these measurement locations than those of location 1-3 and 9 in **Figure 15**.

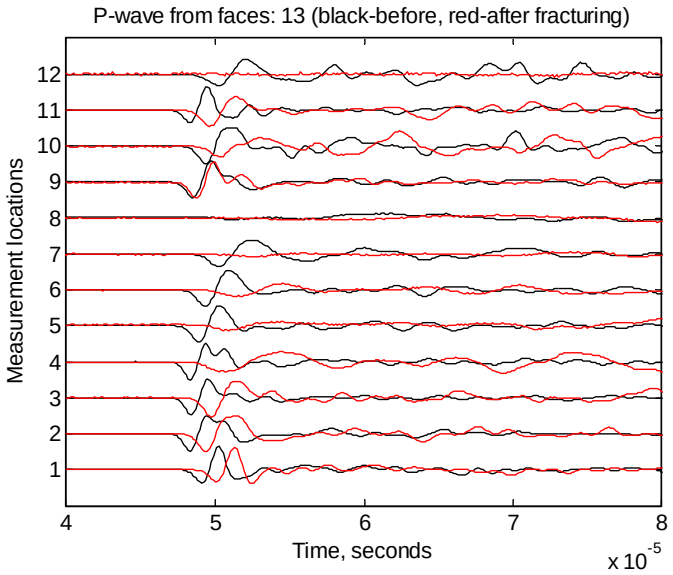

Figure 14 P-wave signatures measured from face 1 & 3 of sample 1.

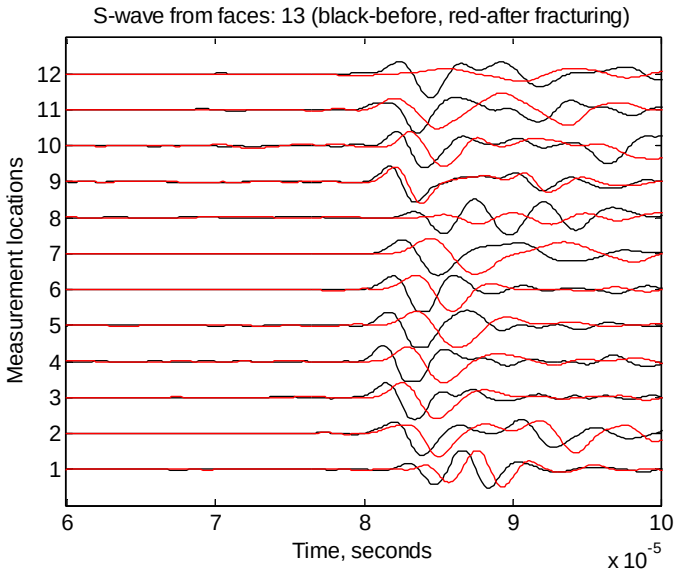

Figure 15 S-wave signatures measured from face 1 & 3 of sample 1.

To present the acoustic measurements more quantitatively, we extracted the arrival time of S-wave signals measured on face 1 & 3 for each sample and calculated the wave velocity, seeing

that S-wave is sensitive to fractures or gas gaps created on its transmission pathway. Note that the minimum horizontal stress or x-stress was exerted on face 1 & 3. **Figure 16** compares the S-wave velocity measured from face 1 & 3 of sample 1 before and after $scCO_2$ injection-induced fracturing. Remarkably retarded velocity at location 3-8 and 10-12 indicates the creation of fracture planes between these locations on face 1 and their corresponding points on face 3. The velocity decrease at location 1, 2, 3, and 9 is caused by compressional damage of tri-axial stress loading and can be a reference for the other locations.

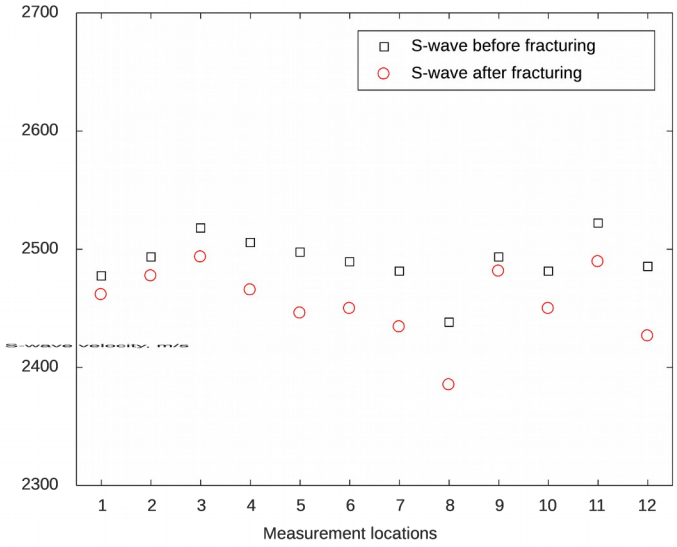

Figure 16 S-wave velocity measured on face 1 & 3 for sample 1.

S-wave velocity values measured on face 1 & 3 for sample 2 to 5 before and after $scCO_2$ injection-induced fracturing are compared in **Figure 17** to **Figure 20**, respectively.

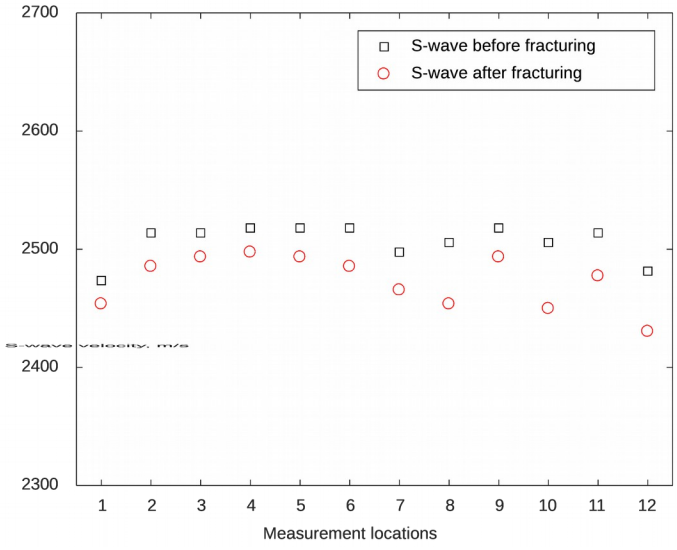

Figure 17 S-wave velocity on face 1 & 3 for sample 2.

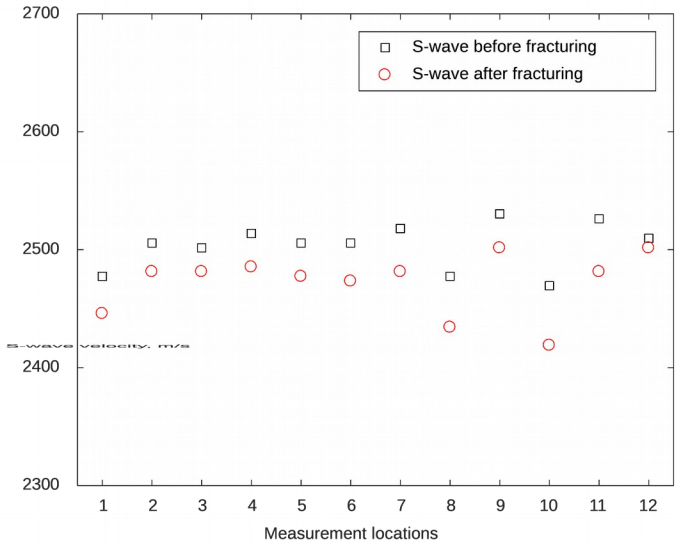

Figure 18 S-wave velocity on face 1 & 3 for sample 3.

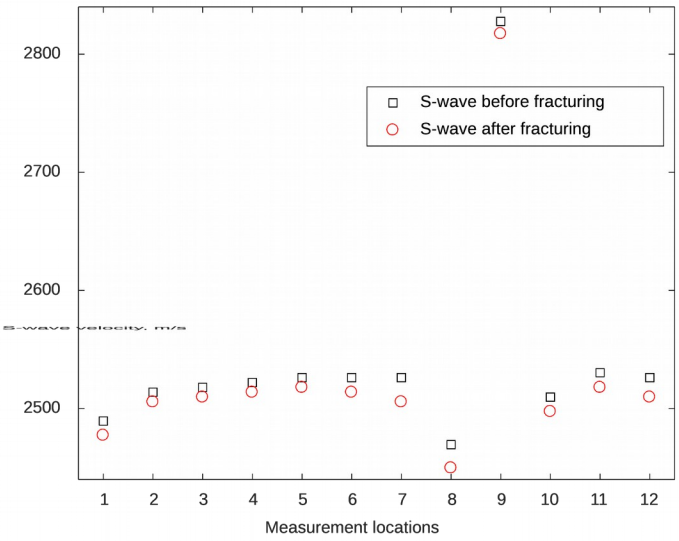

Figure 19 S-wave velocity on face 1 & 3 for sample 4.

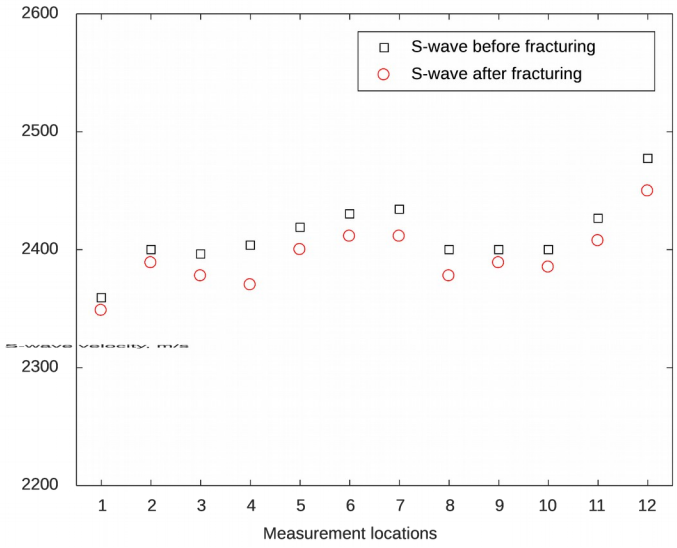

Figure 20 S-wave velocity on face 1 & 3 for sample 5.

Based on the S-wave velocity, we identified the most probable measurement locations and their corresponding points where there are induced-fractures, as summarized in **Table 2**. Locations on face 1 with retarded S-wave velocity could be considered as a conservative map of the fracture planes between face 1 & 3, and the fracture tips probably go beyond them because the tightly closed tip region might be undetectable by the S-wave signals.

Table 2 Acoustic measurement locations on face 1 indicating induced fractures

Concrete sample #	Locations with normal S-wave velocity	Locations with retarded S-wave velocity
1	1-3, 9	4-8, 10-12
2	1, 3, 4, 9	2, 5-8, 10-12
3	1-3, 9, 12	4-8, 10, 11
4	1-12	--
5	1-2, 9-10	3-8, 11, 12

Borehole pressure decay

After the $scCO_2$ injection tests, the conductivity of induced fractures inside the concrete samples were quantified by borehole pressure decay tests. Under no confining stress, borehole pressure of the samples was raised to 180 psig by injecting nitrogen gas and then was allowed to decay naturally. The pressure decay curves of five samples are shown in **Figure 21**, demonstrating high fracture conductivity or improved permeability as compared to the pre-injection decay curve, which is almost the same for all samples. Sample 1, 2, and 3 show a trend that as the minimum horizontal stress (x-stress) increases while maintaining the same stress difference, the conductivity of the induced fractures decreases, attributing to the increasing confinement of fracture propagation. In addition, by enlarging the stress difference, fracture conductivity of

sample 5 rises in comparison with sample 2 and 4. Nonetheless, the fracture conductivity of sample 2 and 4 does not follow the same trend, as attributed to experimental uncertainty.

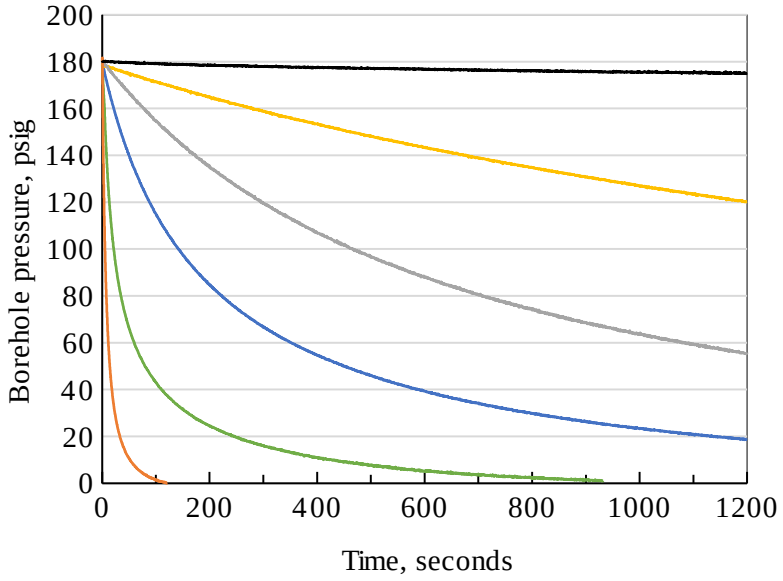

Figure 21 Pressure decay curves of five samples after $scCO_2$ fracturing.

Induced fracture morphology

After the acoustic emission measurements and pressure decay tests, dye solution was injected into the concrete samples to color fractures induced by $scCO_2$ injection. The injection pressure was set at 180 psig to avoid creating new fractures. Afterwards, the samples were broken down by injecting nitrogen gas under originally planned tri-axial stresses to reveal the colored $scCO_2$ induced fractures.

The assembled six faces and the revealed fracture morphology of five concrete samples after dye coloring and gas fracturing are shown in **Figure 22** to **Figure 26**, respectively. In the assembled faces, sample numbers are marked on face 1. Dark dots result from acoustic couplant. Small black arrows indicate the observable fractures after $scCO_2$ injection, and blue color is dye solution that seeped out of induced fractures. On the gas fracture profiles of the broken samples, purple lines circle the $scCO_2$ injection-induced fractures.

As shown in **Figure 22**, blue dye solution seeped out of observable induced fractures propagated to face 2, 4, 5, and 6, showing a major $scCO_2$ injection-induced fracture plane that is perpendicular to the minimum horizontal stress direction (x-axis). This major fracture plane that measures about 48 cm on sample faces is further revealed by the right subgraph of gas fracture planes, which were taken by unfolding the sample from face 2. Nitrogen gas fracturing of sample 1 reached a peak of 1298 psig under tri-axial stress loading. The colored area delineates the $scCO_2$ injection-induced fracture planes that initiated from the uncased section of the borehole and propagated in a rugged manner to the block faces. In area, the induced fractures accounts for

about 3/4 of the whole cross section. Comparison with the acoustic measurement locations shows that the induced fracture plane cut across location 4-8 and 10-12, without interfering with location 1-3 and 9. This observation agrees very well with the derivations from **Figure 14** and **Figure 15**, demonstrating that active acoustic emission measurement is an effective method to detect existing fractures inside concrete blocks.

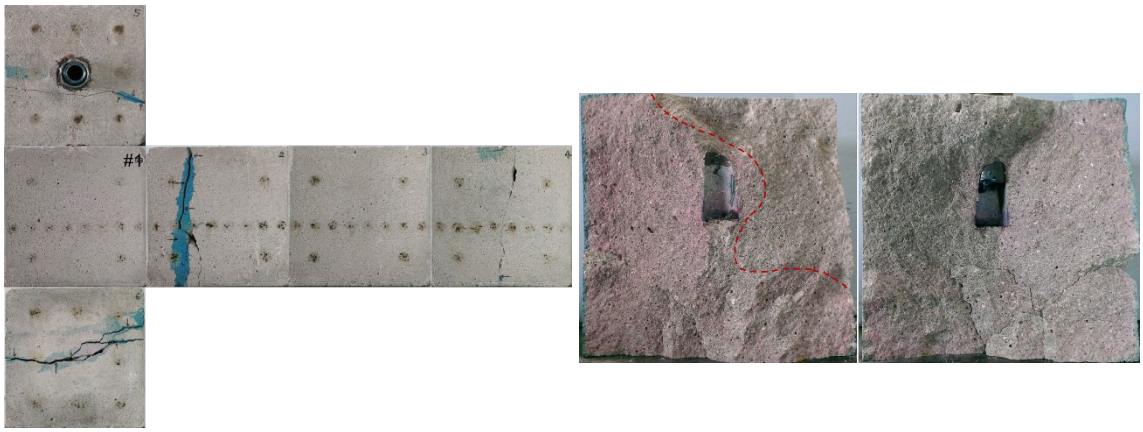

Figure 22 Sample 1 after dye coloring and gas fracturing (Fracture plane opened from face 2).

The $scCO_2$ injection-induced fracture orientation and morphology in sample 2-5 are shown in **Figure 23** to **Figure 26**, respectively. The major characteristics of $scCO_2$ injection-induced fractures including length, smoothness, relative area, and orientation as well as the peak fracturing pressure during $scCO_2$ injection, responses on tri-axial stress at the peak fracturing point, locations with delayed acoustic signatures, and the peak pressure of nitrogen gas fracturing are summarized in **Table 3** for illustration of the $scCO_2$ injection-induced fracturing process and corroboration of the experimental methods.

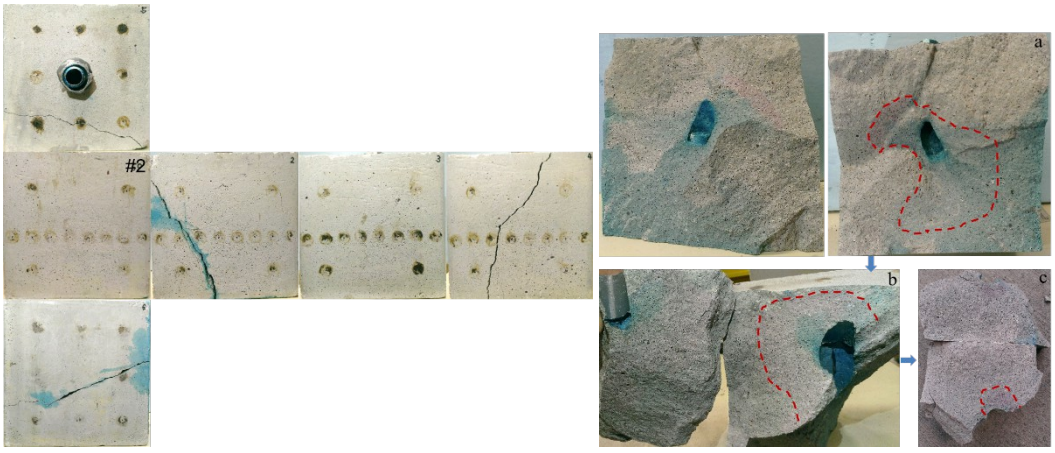

Figure 23 Sample 2 after dye coloring and gas fracturing (Fracture plane *a* opened from face 2).

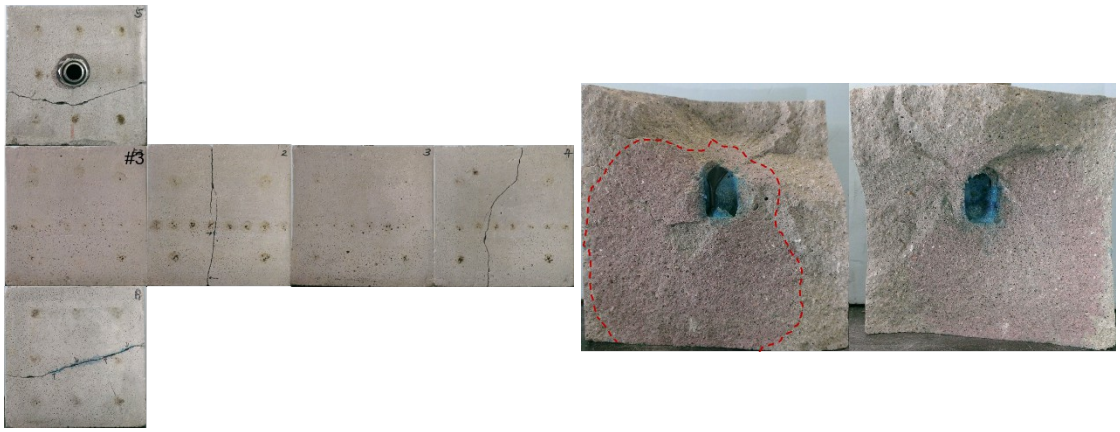

Figure 24 Sample 3 after dye coloring and gas fracturing (Fracture plane opened from face 2).

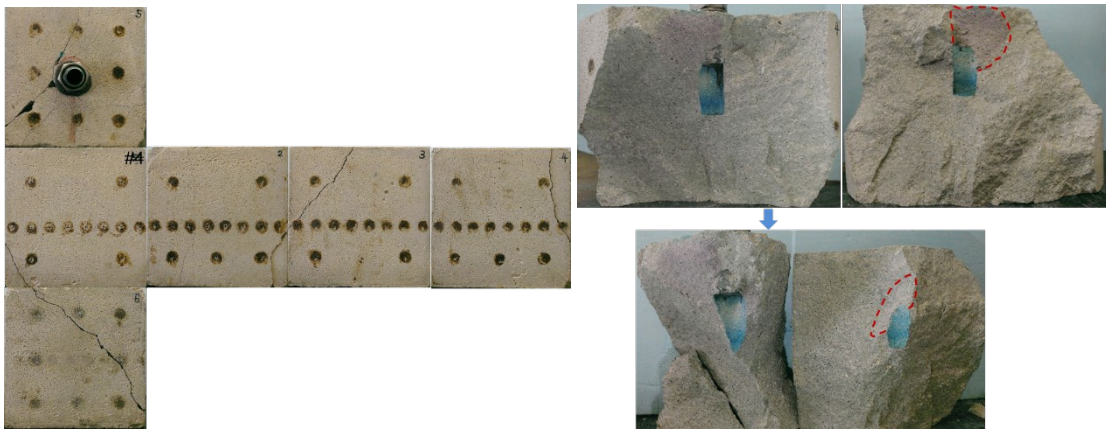

Figure 25 Sample 4 after dye coloring and gas fracturing (Fracture plane opened from face 3).

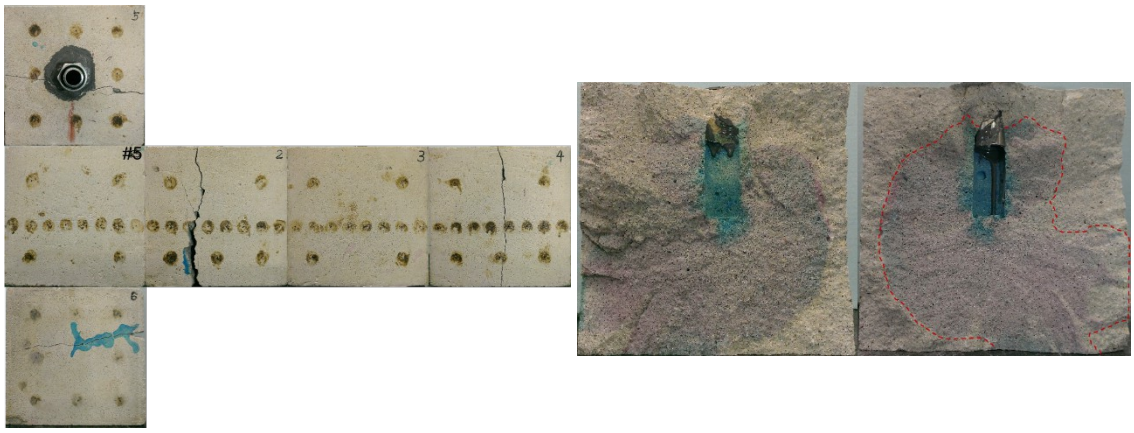

Figure 26 Sample 5 after dye coloring and gas fracturing (Fracture plane opened from face 2).

Table 3 Summary of $scCO_2$ injection-induced fracturing of 5 concrete samples

#	Stress x:y:z psi	$scCO_2$ P psig, T °C	Stress response	Acoustic emission signature	N_2 peak pressure psig	Colored fracture length on surface, Fracture morphology, area, and orientation
1	1000: 1625: 2250	1091.5, 46.8	Obvious	Delayed at 4-8, 10-12	1298	48 cm on face 2, 4, 5, and 6; single rugged fracture, ~3/4 of the cross section, fracture plane perpendicular to x-axis
2	1250: 1875: 2500	1641.2, 34.8	Un-obvious	Delayed at 2, 5-8, 10-12	~1600 (data file corrupted)	32 cm on face 2 & 6, multiple rugged fracture planes, >1/2 of the cross section, the major fracture nearly perpendicular to x-axis, small ones angular to x- and y-axis
3	1500: 2125: 2750	2130.2, 43.6	Obvious	Delayed at 4-8, 10, 11	1719	12 cm on face 2 & 6, single smooth fracture plane around the borehole, ~1/2 of the cross section, perpendicular to x-axis
4	1250: 1562: 1875	1641.9, 45.2	Un-obvious	Not delayed	1614	2 cm on face 5, multiple small rugged fracture planes, upward from borehole, 2” wide, ~1/16 of the cross section, the major fracture is angular to x- and y-axis
5	1250: 2187: 3125	1195.5, 39.9	Obvious	Delayed at 3-8, 11-12	975	18 cm on face 2 & 6, circular slightly rugged fracture around borehole, 7.5” wide, ~2/3 of the cross section, fracture plane perpendicular to x-axis

From the fracture morphology in **Table 3**, results of sample 1-3 show that as confining stress levels increase while stress difference remains constant, length of fractures reaching the block surface decreases and fracture development inside the sample shrank. When the stress difference increases while x-stress remains the same for sample 4, 2, and 5, the length of observed fractures on sample surface tends to first increase and then decrease, whereas the fracture planes developed inside the sample keeps increasing. Given higher confining stress levels and stress differences, the major induced fracture planes become much smoother and are perpendicular to the minimum horizontal stress direction, e.g. sample 3 and 5. On contrary, with low confining stress levels and differences, the fracture planes are more rugged and even branched, and are angular to the minimum horizontal stress direction. By reducing the stress difference to 312 psi for sample 4, the fracture growth does not seem to be dominated by the stress field at all.

In addition, for all five samples the induced fracture planes colored and revealed by nitrogen gas fracturing overlap well with the mapping of arrival time delays in acoustic waves, although the measurement locations chosen for acoustic emission are not sufficient to detect the boundary of the induced fractures. Moreover, induced fracture orientations are also directly reflected by the responses on tri-axial stress profiles during the $scCO_2$ injection experiments. Once there were big fractures initiating and propagating perpendicular to the minimum horizontal stress, a noticeable hump showed up on x-stress, e.g. sample 1, 3, and 5. Otherwise, no obvious changes could be seen on stress profiles, e.g. sample 2 and 4. Another noteworthy point is that, in **Figure 22** to **Figure 26**, the outer uncolored fractures created by N_2 fracturing are obviously more wavy with much higher roughness than colored $scCO_2$ fractures, as a result of the lower N_2 viscosity. For example, viscosity of N_2 at 20.0 ºC and 1500 psia is 19.77 μPa·s and that of $scCO_2$ at 40.0 ºC and 1500 psia is 50.33 μPa·S (NIST, 2017). Lower viscosity enables fluids to penetrate or leak-off

into localized pores or microfractures more easily, hence posing higher probability for major fractures to divert and branch off into these directions. This viscosity dependent fracture behavior has also been observed by Ishida et al. (2004) and Li et al. (2016).

Breakdown pressure analysis

The concrete sample broke down at the point the $scCO_2$ injection pressure reached the highest peak, i.e. the breakdown pressure. As reviewed at the beginning, the breakdown pressure of non-poroelastic rocks can be predicted using equation (1) and that of poroelastic rocks can be predicted using equation (2). In these experiments, pore pressure is negligible, Biot's constant α is taken as 0.70, and Poisson's ratio υ is 0.24 for these concrete samples [Yao 2016]. Then by substituting the real tri-axial stresses exerted on the samples when they were broken down and adjusting the tensile strength within the experimental measurement range into (2), the predicted breakdown pressure values are obtained, as scattered with the experimental data in **Figure 27**. The tensile strength used in equation (1) for upper bound breakdown pressure calculation adopted the average value of 473 psi. Parameters used in equation (2) for matching the experimental data are listed in **Table 4**. The relative deviations of experimental data from predictions are within ±10%. It is obvious that although these caprock-analogous concrete samples have very low average porosity and permeability (< 10% and < 10 micro-Darcy), they are remarkably different from non-poroelastic rocks and showed much lower breakdown pressure in $scCO_2$ injection cases.

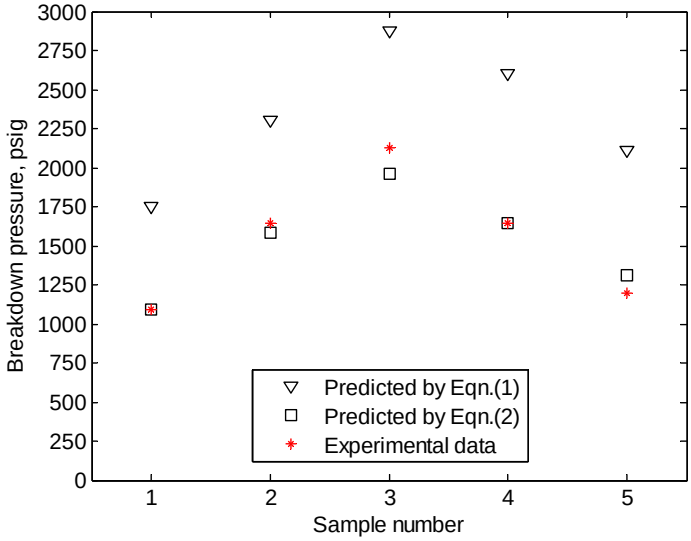

Figure 27 Breakdown pressure from experiments and predicted by equation (1) and (2).

Table 4 Parameters used in equation (2) for experimental data matching

Sample	tri-axial stresses x:y:z psi	Tensile strength psi		P_b from eqn. (2)	P_b from Exp.	Dev. %
1	940.5:1547.8:2215.5	386	Biot constant	1148.4	1091.5	0.03

2	1238.1:1883.1:2500.3	576	α = 0.70	1514.9	1641.2	3.70
3	1492.1:2075.6:2742.0	576		1889.3	2130.2	8.85
4	1229.6:1558.0:1900.7	366 356	Poisson's	1711.8	1641.9	0.02
5	1269.9:2175.4:3107.3		ratio υ = 0.24	1385.3	1195.5	-8.63

IV. Conclusions

In-depth understanding of occurrence of CO_2 injection-induced fracturing are essential for robust CO_2 geological sequestration design and optimum operations. This study developed fundamental understandings of injection-induced geomechanical effects on supercritical CO_2 storage systems, including fracturing processes, fracture morphology, and breakdown pressure correlations by laboratory studies on caprock analogs. Based on the foregoing analyses of the $scCO_2$ injection experiments, the following conclusions can be drawn.

1) Supercritical CO_2 injection-induced fracturing usually occurred and accomplished instantaneously in laboratory homogeneous caprock analogs, without showing recognizable fracture propagation stages. Induced fracturing is strongly controlled by the heterogeneities in the tri-axial stress conditions and is affected by low viscosity of $scCO_2$. Fractures generated are generally large, simple, and relatively smooth, and their planes are approximately perpendicular to the minimum horizontal stress, given high stress differences and stress levels. While at relatively low confining stresses with small stress differences, multiple small fractures branch off the borehole in arbitrary directions and fracture planes are rough. Nonetheless, in field implementations, fracture propagation is still expected to be quasi-static in terms of high surrounding pressure.

2) Occurrence of breakdown or fracture initiation from borehole into rock matrix can be identified from the $scCO_2$ injection pressure profile, associating with temperature drop due to vaporization. Acoustic wave signatures provide a nondestructive means to map the domain of fractures generated in invisible rock samples. Dye coloring and gas fracturing visually revealed the morphology and boundary of induced fractures.

3) Non-poroelastic mechanics model substantially overestimates the breakdown pressure of low porosity and low permeability concrete blocks when $scCO_2$ is the injected fluid, probably due to that $scCO_2$ has a low viscosity and therefore high leak-off rate. Provided additional parameters, the poroelastic mechanics model can satisfactorily match the experimental data.

4) Low breakdown pressure, hardly to be trapped in micro-pores, and miscibility with hydrocarbons enable $scCO_2$ or liquid CO_2 an advantageous fracturing fluid to water and oil based fracturing fluids in stimulating unconventional oil and gas reservoirs, especially considering that ultralight proppants are becoming industrially available.

These laboratory experiments deepen our understandings of $scCO_2$ injection-induced fracturing in reservoir caprocks, provide useful findings for assessing CO_2 geologic storage reservoir

conditions, and are instructive for enhancing the performance of life cycle storage operations. In particular, the calibrated poroelastic mechanics model can be incorporated into reservoir simulators that couple geomechanics (e.g. TOUGH2-CSM [Winterfeld et al. 2012] and TOUGH-FLAC [Rutqvist 2011]) to simulate field-scale CO_2 injection-induced rock mechanical processes and ensure safe and permanent CO_2 sequestration and storage in reservoirs. This will also enable us to quantify potential leakage pathways as well as to develop remediation measures when needed in these reservoirs. To upscale laboratory-scale scCO_2 injection-induced fracturing findings to field-scale applications, more complex factors should be taken into account, for example, rock heterogeneity, existing natural fractures or faults, reservoir boundary conditions, etc. Thermal effects resulted from expansion of CO_2 might play an important role as well.

Acknowledgement

The authors thank the financial support from National Energy Technology Laboratory of US Department of Energy (Quantitative Characterization of Impacts of Coupled Geomechanics and Flow on Safe and Permanent Geological Storage of CO_2 in Fractured Aquifers, Project Number: DE-FE0023305) and Foundation CMG.

Reference

Alqahtani, N. B., 2015. Experimental study and finite element modeling of cryogenic fracturing in unconventional reservoirs, Doctoral dissertation, Colorado School of Mines.

Alqahtani, N. B., Cha, M., Yao, B., Yin, X., Kneafsey, T. J., Wang, L., Wu, Y.-S. and Miskimins, J. L., 2016, May. Experimental Investigation of Cryogenic Fracturing of Rock Specimens Under True Triaxial Confining Stresses. In SPE Europec featured at 78th EAGE Conference and Exhibition. SPE-180071-MS.

Bissell, R.C., Vasco, D.W., Atbi, M., Hamdani, M., Okwelegbe, M. and Goldwater, M.H., 2011. A full field simulation of the In Salah gas production and CO_2 storage project using a coupled geo-mechanical and thermal fluid flow simulator. Energy Procedia, 4, pp.3290-3297.

Bunger, A. P., Jeffrey, R. G., Detournay, E., 2005. Application of scaling laws to laboratory-scale hydraulic fractures, 40th US Symposium on Rock Mechanics, June 25-29, Anchorage, Alaska, USA.

Cha, M., Alqahtani, N.B., Yao, B., Yin, X., Wu, Y.-S. and Kneafsey, T. J. 2016. Development of laboratory system for cryogenic fracturing study. Energy Geotechnics, pp. 381-388.

Daneshy, A.A., 1978. Hydraulic fracture propagation in layered formations, SPE Journal. 18:33-41.

Detournay, E.E. and Cheng, A.E., 1992, January. Influence of pressurization rate on the magnitude of the breakdown pressure. In the 33th US Symposium on Rock Mechanics (USRMS). American Rock Mechanics Association.

Detournay, E. and Cheng, A.H.D., 1993. Fundamentals of poroelasticity 1. Chapter 5 in Comprehensive Rock Engineering: Principles, Practice and Projects, II, pp.113-171.

DOE, 2014. Carbon storage technology program plan.

Ehlig-Economides, C.A., Anchliya, and Song, B., 2010. Pressure falloff test interpretation for leakage detection during CO_2 injection in a deep saline aquifer, presented at the SPE EUROPEC/EAGE Annual Conference and Exhibition held in Barcelona, Spain, June 14-17.

Gupta, D.V.S. and Bobier, D.M., 1998. The history and success of liquid CO_2 and CO_2/N_2 fracturing system. SPE, 40016, pp.15-18.

Gupta, D.V.S., Niechwiadowicz, G. and Jerat, A.C., 2003, January. CO_2 Compatible Non-Aqueous Methanol Fracturing Fluid. In SPE Annual Technical Conference and Exhibition. SPE-84579-MS.

Haimson, B. and Fairhurst, C., 1967. Initiation and extension of hydraulic fractures in rocks. SPE Journal, 7(03), pp.310-318.

Huang, Z. Q., Winterfeld, P. H., Xiong, Y., Wu, Y.-S. and Yao, J., 2015. Parallel simulation of fully-coupled thermal-hydro-mechanical processes in CO_2 leakage through fluid-driven fracture zones. International Journal of Greenhouse Gas Control, 34, pp. 39-51.

Hubbert, M. K. and Willis, D. G., 1957. Mechanics of hydraulic fracturing.

Ishida T., Chen, Q., Mizuta, Y. and Roegiers, J.-C. 2004. Influence of fluid viscosity on the hydraulic fracturing mechanism. Journal of Energy Resources Technology, 126, pp.190-200.

Ishida, T., Aoyagi, K., Niwa, T., Chen, Y., Murata, S., Chen, Q. and Nakayama, Y., 2012. Acoustic emission monitoring of hydraulic fracturing laboratory experiment with supercritical and liquid CO_2. Geophysical Research Letters, 39(16).

Lee, J., K. B. Min, and J. Rutqvist, J., 2012. Evaluation of leakage potential considering fractures in the caprock for sequestration of CO_2 in geological media, presented at the 46th US Rock Mechanics/Geomechanics Symposium held in Chicago, IL, USA, June 24-27.

Leung D. Y. C., Caramanna, G. and Maroto-Valer, M. M. 2014. An overview of current status of carbon dioxide capture and storage technologies. Renewable and Sustainable Energy Reviews, 39, pp. 426-443.

Li, X., Feng, Z., Han, G., Elsworth, D., Marone, C., Saffer, D. and Cheon, D.S., 2016. Breakdown pressure and fracture surface morphology of hydraulic fracturing in shale with H_2O, CO_2 and N_2. Geomechanics and Geophysics for Geo-Energy and Geo-Resources, 2(2), pp.63-76.

Lillies, A.T. and King, S.R., 1982, January. Sand fracturing with liquid carbon dioxide. In SPE Production Technology Symposium. SPE-11341-MS.

NIST, 2017. Thermophysical properties of fluid systems. <http://webbook.nist.gov/chemistry/fluid/>, retieved April 14, 2017.

Rhino, K., Loisy, C., Cerepi, A., Garcia, B., Rouchon, V., Noirez, S., Le Gallo, C., Delaplace, P., Willequet, O., Bertrand, C. and El Khamlichi, A., 2016. The Demo-CO_2 project: Monitoring and comparison of two shallow subsurface CO_2 leakage experiments with gas tracer associated in the carbonate vadose zone. International Journal of Greenhouse Gas Control, 53, pp. 207-221.

Rinehart, A.J., Dewers, T.A., Broome, S.T. and Eichhubl, P., 2016. Effects of CO_2 on mechanical variability and constitutive behavior of the Lower Tuscaloosa Formation, Cranfield Injection Site, USA. International Journal of Greenhouse Gas Control, 53, pp.305-318.

Rillard, J., Loisy, C., Le Roux, O., Cerepi, A., Garcia, B., Noirez, S., Rouchon, V., Delaplace, P., Willequet, O. and Bertrand, C., 2015. The DEMO-CO_2 project: A vadose zone CO_2 and tracer leakage field experiment. International Journal of Greenhouse Gas Control, 39, pp. 302-317.

Rinaldi, A., and Rutqvist, J., 2013. Modeling of deep fracture zone opening and transient ground surface uplift at KB-502 CO_2 injection well, In Salah, Algeria, International Journal of Greenhouse Gas Control, 12, pp. 155-167.

Rutqvist J., 2011. Status of the TOUGH-FLAC simulator and recent applications related to coupled fluid flow and crustal deformations. Computers & Geosciences, 37, pp. 739-750.

Schmitt, D. R. and Zoback, M. D., 1992. Diminished pore pressure in low-porosity crystalline rock under tensional failure: Apparent strengthening by dilatancy. Journal of Geophysical Research: Solid Earth, 97(B1), pp.273-288.

Sinal, M. L. and Lancaster, G., 1987. Liquid CO_2 fracturing: Advantages and limitations. Journal of Canadian Petroleum Technology, 26(05).

Stoeckhert, F., Molenda, M., Brenne, S. and Alber, M., 2015. Fracture propagation in sandstone and slate-Laboratory experiments, acoustic emissions and fracture mechanics. Journal of Rock Mechanics and Geotechnical Engineering, 7(3), pp. 237-249.

Suehiro, Y., Nakajima, M., Yamada, K. and Uematsu, M., 1996. Critical parameters of $\{xCO_2+(1-x)\ CHF_3\}$ for x = (1.0000, 0.7496, 0.5013, and 0.2522). The Journal of Chemical Thermodynamics, 28(10), pp. 1153-1164.

Wang, L., Yao, B., Cha, M., Alqahtani, N. B., Patterson, T. W., Kneafsey, T. J., Miskimins, J. L., Yin, X. and Wu, Y.-S., 2016. Waterless fracturing technologies for unconventional reservoirs-opportunities for liquid nitrogen. Journal of Natural Gas Science and Engineering, 35, pp.160-174.

Wang, S., Huang, Z., Wu, Y.-S., Winterfeld, P. H. and Zerpa, L. E., 2016. A semi-analytical correlation of thermal-hydraulic-mechanical behavior of fractures and its application to modeling reservoir scale cold water injection problems in enhanced geothermal reservoirs. Geothermics, 64, pp. 81-95.

Warpinski, N. R., Clark, J. A., Schmidt, R. A. and Huddle, C. W., 1982. Laboratory investigation on the-effect of in-situ stresses on hydraulic fracture containment. SPE Journal, 22(03), pp. 333-340.

Weijers, L., de Pater, C. J., Hagoort, J. 1996. A new mechanism for hydraulic fracture initiation, the 2nd North American Rock Mechanics Symposium, June 19-21, Montreal, Quebec, Canada.

Winterfeld, P. H., Wu, Y.-S., Pruess, K. and Oldenburg, C. 2012. Development of Advanced Thermal-Hydrological-Mechanical Model for CO_2 Storage in Porous and Fractured Saline Aquifers, presented at TOUGH Symposium 2012, Lawrence Berkeley National Laboratory, CA, September 17-19.

Yao, B., 2016. Experimental study and numerical modeling of cryogenic fracturing process on laboratory-scale rock and concrete samples. Master’s thesis, Colorado School of Mines.

Yao, B., Wang, L., Yin, X. and Wu, Y.-S., 2016. Numerical modeling of cryogenic fracturing process on laboratory-scale Niobrara shale samples. Journal of Natural Gas Science and Engineering.